AIMS Energy, 9(4): 842–853.
DOI: 10.3934/energy.2021039
Received: 31 January 2021
Accepted: 23 June 2021
Published: 29 June 2021

http://www.aimspress.com/journal/energy

Research article

Numerical design of dual-scale foams to enhance radiation absorption

Hong-Wei Chen[1], Fu-Qiang Wang[2], Yang Li[1,*], Chang-Hua Lin[1], Xin-Lin Xia[3] and He-Ping Tan[3]

[1] College of Petroleum Engineering, Liaoning Petrochemical University, Fushun 113001, China
[2] School of New Energy, Harbin Institute of Technology at Weihai, Weihai 264209, China
[3] School of Energy Science and Engineering, Harbin Institute of Technology, Harbin 150001, China

* **Correspondence:** Email: liyang@lnpu.edu.cn; Tel: +8618846070129.

Abstract: Unlike silicon carbide ceramic, the alumina ceramic and zirconia ceramic are by its very nature weakly absorbing in visible and near infrared wavebands. Therefore, open-cell foams made of such ceramics are rarely used in applications requiring strong absorption of radiation energy, such as solar absorbers. In order to improve the potential of such foams, open-cell foams with dual-scale pores were digitally designed in the limit of geometric optics. The first-order pores are obtained by Voronoi tessellation technique and then the second-order pores are realized by the design of 'porous strut'. A Monte Carlo Ray-tracing method is applied in the dual-scale foam structure for radiative transfer calculation. The parameterized study is conducted on the radiation absorption of alumina foam sheets and zirconia foam sheets. The results show that for the present cases, the designed dual-scale alumina foams with strut porosity p_s = 0.3 can increase the normal absorptance within the wavebands from 0.4 μm to 7.0 μm by 62.7% than the foams with single-scale pores. For the zirconia foams, this increase is 115.9% within the wavebands from 1.2 μm to 7.6 μm. The findings can provide strong confidence on dual-scale foams to enhance the absorption of radiation energy in potential applications.

Keywords: structure design; dual-scale foam (DSF); porous strut; radiation; semitransparent

Nomenclature: A_N: normal absorptance; d_c: diamter of cell, mm; d_h: diameter of concave hemisphere, mm; I: radiation intensity, W m^{-2} sr^{-1}; I_b: blackbody radiation intensity, W m^{-2} sr^{-1}; L_f: foam thickness, mm; l_r: reflection path, mm; l_e: extinction path, mm; n: refractive index; p_f: porosity of foam; p_s: porosity of strut; q: radiative heat flux, W m^{-2}; R_{NH}: normal-hemispherical reflectance; $\vec{r}$: position vector; $\vec{s}$: propagation direction vector; T_{NH}: normal-hemispherical transmittance; V_s^a: apparent volume of strut, mm^3; V_s^r: real volume of strut, mm^3

Greek symbols: β: extinction coefficient of solid phase, mm^{-1}; γ: angle degree; κ: absorption coefficient of solid phase, mm^{-1}; λ: wavelength, μm; ξ: random number; ρ: reflectivity; σ_s: scattering coefficient of solid phase, mm^{-1}; Φ: scattering phase function of solid phase, sr^{-1}; Ω': solid angle, sr
Subscripts: a: absorbed; in: incident; r: reflected; s: strut; t: transmitted; λ: spectral
Acronyms: DSF: dual-scale foam; MCRT: Monte Carlo Ray-tracing; μ-CT: micro-computed tomography; GOA: geometric optics approximation

1. Introduction

Thermal radiation plays a key role in energy applications at high temperature, since the radiative transfer becomes the considerable energy conversion mode due to temperature increasing [1–3]. To enhance the energy conversion, a kind of porous materials called open-cell foams are usually used in practice [4–6]. Open-cell foams are commonly composed of interconnected ligaments or called struts which are made of metals, ceramics, carbon and so on [7,8]. Thanks to the porous structure of foams, the incident radiation can be absorbed volumetrically throughout the whole material, which improves the efficiency of energy conversion [9–11].

The factors that affect the radiation absorption of foam materials can be attributed to porous structure and component material properties [12,13]. The porous structure is described by the structural parameters such as porosity, pore size (sometimes called pore density) and strut shape factor [14,15]. The way to obtain digital foam structure includes micro-computed tomography (μ-CT) technique and artificial reconstruction technique [16]. In recent years, more and more attention has been paid to artificial reconstruction technique which is more flexible and allows parameterized study [17]. With the development of advanced manufacturing technique such as 3D printing, foam materials with special designed structure (means having specific physical/chemical functions) are coming out [18]. Artificial reconstruction is based on different cell models [19], such as cube model, Kelvin model, Weaire-Phelan model, and Voronoi model. Among them, the Voronoi model is closer to the real foam structure, because its cell model is random and statistically consistent with the real foam [20]. In order to maximize the radiative heat transfer of foam materials in the tube, Pelanconi et al. [21] designed and 3D printed a set of alumina ceramic foams with radial gradient cells. Numerical and experimental results showed that the ceramic foams with radial shrinkage cells has better radiation absorption and higher temperature inside the materials. Furler et al. [22] designed and manufactured a set of CeO_2 foams with dual-scale pores, as shown in Figure 1, to accelerate the thermal cracking of CO_2. It was found that the reaction speed is increased by at least one order of magnitude due to the porous struts. In short, foam structure design has become a very valuable and promising research field.

In practice, the foams made of strongly absorbing materials such as silicon carbide ceramic are widely popular for radiation absorption [23,24]. However, different from silicon carbide ceramic [25], the alumina ceramic and zirconia ceramic are by its very nature weakly absorbing within visible and near infrared wavebands [26]. Therefore, such ceramic foams are rarely used in applications requiring strong absorption of radiation energy, such as solar absorbers [27,28]. In order to expand the potential of such foams, this work aims to digitally design dual-scale ceramic foams in the limit of geometric optics. The paper was organized as follows. In section 2.1, dual-scale foams were designed based on the Voronoi cell model, and then the porous struts were defined for parameterized study. In section 2.2, a Monte Carlo Ray-tracing (MCRT) method accelerated by octree algorithm

was developed for radiative transfer calculation. In sections 3.1 and 3.2, the radiation absorption of alumina foam sheets and zirconia foam sheets was analyzed, respectively.

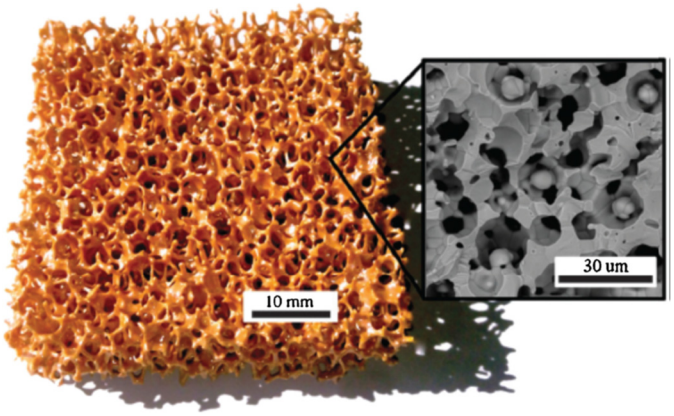

Figure 1. Ceramic foams with dual-scale pores [22].

2. Numerical methods

2.1. Design of dual-scale foams

As shown in Figure 1, dual-scale foams have a classical porous morphology such as pores at several millimeters, but their struts are still also porous with pores at dozens of microns. Therefore, the structure construction of digital dual-scale foams contains two levels. The first order is the classical foam morphology including open cells and interconnected struts. The second order is the porous struts with smaller holes. The design of dual-scale foams are conducted by Voro++ and SolidWorks software. First, we use open source Voro++ software to perform the Voronoi tessellation to generate a cellular structure composed of solid struts. Then, the SolidWorks software with Application Program Interface (API) is used to modify the solid struts to obtain second-order pores. In the generation of first-order structure, as shown in Figure 2, a random dense packing of spheres with a log-normal distribution of sphere volumes are first generated and distributed irregularly within a given box. Then the Voronoi tessellation is performed to transform this cube box into a cellular structure. Last, open-cell foams are obtained by generating solid struts along the cell edges i.e., between the neighbor cell vertices. For typical open-cell foams, porosity p_f and cell diameter d_c are the main structural parameters in the generation of Voronoi foam, as defined in Ref. [19].

Since the present work focuses on the influence of porous struts, the cylindrical struts rather than the ones with complex shape as defined in our recent work [15] are used. Inspired by the porous struts shown in Figure 1, a set of porous struts were designed as shown in Figure 3. The struts were dug regularly with concave hemisphere. In order to satisfy geometric optics as much as possible, the diameter of concave hemisphere is given as a much bigger value d_h = 200 μm compared to the investigated wavebands. Furthermore, a structural parameter called 'strut porosity' p_s was defined to characterize the porous struts,

$$p_s = 1 - \frac{V_s^r}{V_s^a} \tag{1}$$

where V_s^a is the apparent volume of a strut (containing the volume of concave hemisphere), and V_s^r is the real volume of a strut (not containing the volume of concave hemisphere). Obviously, the quantity of strut porosity p_s has a physical sense similar to that of foams and varies from zero to a value less than 1 (in fact far less than 1 due to structural strength requirements).

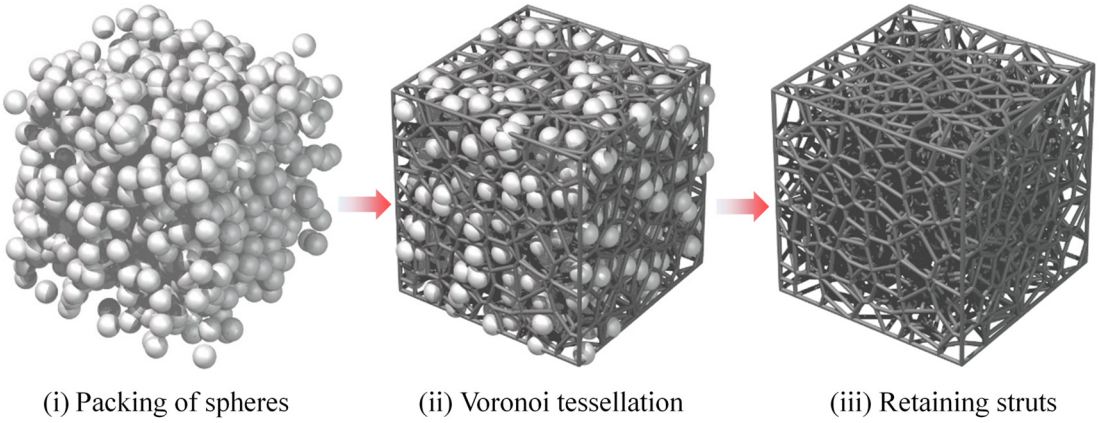

Figure 2. Key steps to build foam structures based on Voronoi tessellation technique.

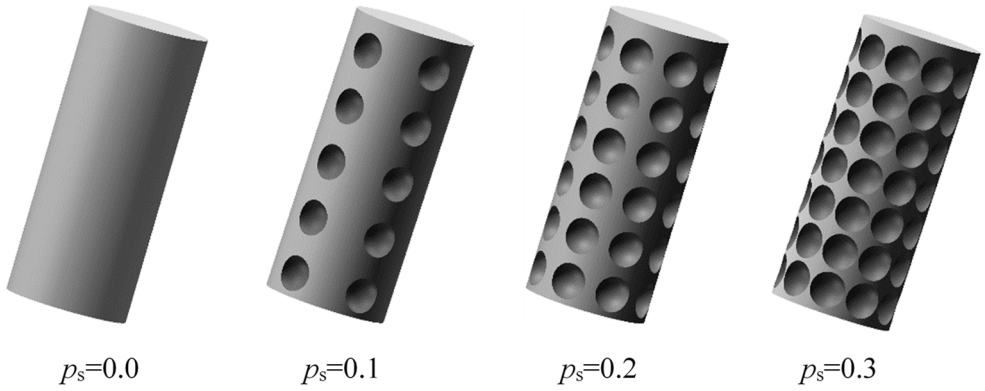

Figure 3. View of porous struts with different strut porosities.

2.2. MCRT method for radiative transfer calculation

The assumptions and principles of the in-house MCRT code have been detailed in our recent papers [29,30]. Here is a brief introduction. The assumptions include geometric optics approximation (GOA), isothermal foam sheet, transparent void phase, absorbing-scattering semitransparent solid phase (i.e., strut), isotropic scattering inside the solid phase, and smooth solid surface. Based on these assumptions, the MCRT method considers the radiative transfer equation (RTE) in the direction $\vec{s}$ as a field equation,

$$\vec{s}\cdot\nabla I_\lambda(\vec{r},\vec{s})+\beta_\lambda I_\lambda(\vec{r},\vec{s})=\kappa_\lambda I_{b\lambda}(\vec{r},T)+\frac{\sigma_{s\lambda}}{4\pi}\int_0^{4\pi} I_\lambda(\vec{r},\vec{s}')\Phi(\vec{r},\vec{s}',\vec{s})d\Omega' \tag{2}$$

where $\vec{r}$ is the position vector, $\vec{s}$ is the propagation direction vector, $\vec{s}'$ is the incoming direction

vector, Φ is the scattering phase function, Ω' is the solid angle, I_λ is the spectral radiation intensity, $I_{b\lambda}$ is the blackbody intensity given by the Planck function, and κ_λ, $\sigma_{s\lambda}$ and β_λ are respectively the spectral absorption, scattering and extinction coefficients, with $\beta_\lambda = \kappa_\lambda + \sigma_{s\lambda}$.

The physical model was illustrated in Figure 4. Special attention should be paid on a single strut in which the radiative transfer is quite complicated. Reflection and refraction occur at the semitransparent strut surface, and meanwhile, extinction, scattering and absorption happen inside the tiny strut. The calculation of reflection and refraction relies on the Fresnel reflection equation [31]. The calculation of extinction, scattering and absorption relies on the media radiation transfer theory [32]. The incident radiative flux (q_{in}, red rays) is assumed to be uniform, collimated and normal to the inlet face of the computational domain. This two-phase domain is compose of transparent void phase (Phase 1) and semitransparent solid phase (Phase 2). Since the refractive index of solid phase n_2 differs from that of void phase n_1, specular reflection and Snell-type refraction take place at the solid-void interface. The local specular reflectivity can be calculated using the Fresnel reflection equation,

$$\rho_s = \frac{1}{2}\left[\frac{\tan^2(\gamma_{in}-\gamma_t)}{\tan^2(\gamma_{in}+\gamma_t)} + \frac{\sin^2(\gamma_{in}-\gamma_t)}{\sin^2(\gamma_{in}+\gamma_t)}\right] \tag{3}$$

where γ_{in} is the incident angle, and γ_t is the refractive angle. The refractive direction of the transmitted ray is given by Snell's law,

$$\sin\gamma_t = \frac{1}{n}\sin\gamma_{in} \tag{4}$$

In the Monte Carlo tests, a random number $\xi_\rho \in (0, 1)$ is generated to determine whether the ray is reflected or refracted,

$$\xi_\rho < \rho_s, \text{ reflected} \tag{5a}$$

$$\xi_\rho > \rho_s, \text{ refracted} \tag{5b}$$

When the ray enters into the semitransparent solid phase, the transmission, absorption and scattering events (as shown in insert of Figure 4) are determined according to the media radiation transfer theory. A possible transfer distance l_{e2} is first calculated by the following probability expression,

$$l_{\beta 2} = -\ln(1-\xi_\beta)/\beta_2 \tag{6}$$

where β_2 is the extinction coefficient of solid phase ($\beta_2 = \kappa_2 + \sigma_{s2}$), and ξ_β is a random number which ranges from 0 to 1 uniformly. When the travel distance $l_{\beta 2}$ is reached, another random number ξ_ω is generated to decide whether the ray is scattered or absorbed, with $\omega_2 = \sigma_{s2}/\beta_2$ being the scattering albedo of solid phase,

$$\xi_\omega < \omega_2, \text{ scattered} \tag{7a}$$

$$\xi_\omega > \omega_2, \text{ absorbed} \tag{7b}$$

where if the ray is scattered, it will continue to travel on into a new direction determined by the isotropic scattering phase function $\Phi_2 = 1$; if absorbed, it is recorded and a new ray is emitted. The incident rays experience multiple reflection-refraction-scattering-absorption process inside the foams until they exit from the foam sheet through the upper surface or through the lower surface, or until

they are absorbed by the solid phase.

In particular, it is assumed that the computational domain is symmetrically continued in the lateral directions, thus simulating an infinite foam slab, as claimed in Ref. [33]. Thus, the lateral sides are assumed to be symmetrical boundaries for radiation, which means 'limited specular reflection'. If the rays hit the lateral sides, a specular reflection will happen with limited reflection path $l_r = l_e - l_r'$, where l_e is the total extinction path of the current ray and l_r' is the path from the starting point to the hitting point.

By tracking the rays, the normal-hemispherical transmittance T_{NH}, normal-hemispherical reflectance R_{NH}, and normal absorptance A_N of the foam sheet can be defined as,

$$T_{NH} = \frac{q_t}{q_{in}} \tag{8}$$

$$R_{NH} = \frac{q_r}{q_{in}} \tag{9}$$

$$A_N = \frac{q_a}{q_{in}} \tag{10}$$

where q presents the radiation energy contained by corresponding rays.

Since the present digital foam has an extremely complex structure, the MCRT calculation may consume quite a lot time. To accelerate the computation, an octree algorithm is combined with the MCRT algorithm, as illustrated in Figure 5. The computational domain is divided into eight equal parts in each partition operation. Accordingly, the solid phase, which means the meshes, is divided into different sub-box. When a ray transmission starts, a simple pre-calculation is firstly conducted to determine the potential path. The sub-boxes that are not in the potential path will not be considered in the MCRT calculation. In this way, the number of meshes to be calculated in MCRT will be greatly reduced. Thus, the computation speed can be accelerated the by nearly two orders of magnitude according to our work [34].

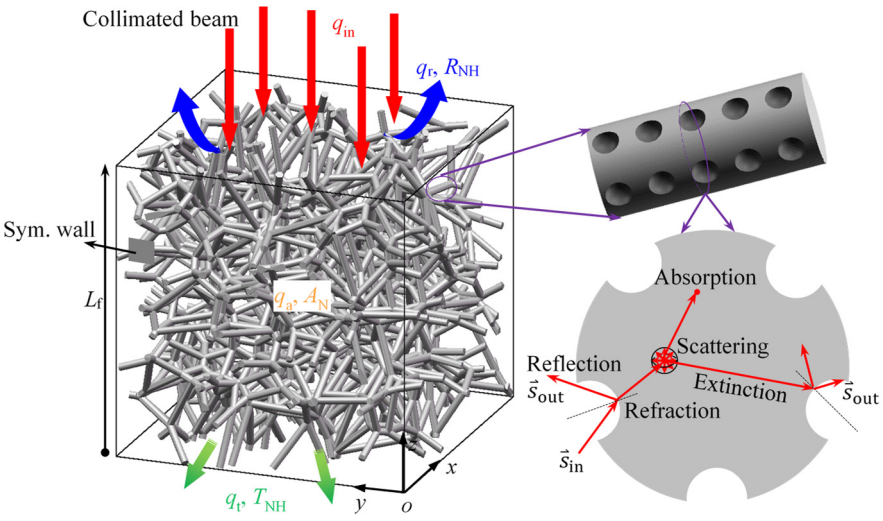

Figure 4. Illustration of typical ray paths in Voronoi foams at different scales.

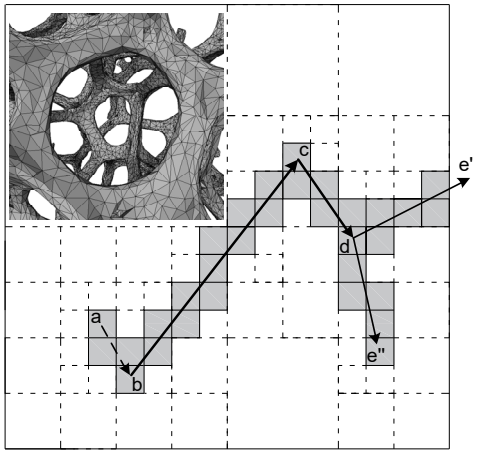

Figure 5. 2D schematic of combining MCRT method and octree algorithm.

3. Results and discussion

In the following, sections 3.1 and 3.2 investigate the apparent radiative properties of alumina and zirconia foam sheets, respectively. The enhance of radiation absorption due to dual-scale pores is particularly discussed. The optical and radiative properties of component materials (refractive index, absorption coefficient, and scattering coefficient) are necessary for radiation transport calculation. One uses the material properties of alumina ceramics from Yang et al. [35] ranging from wavelength 0.4 μm to 7 μm. The material properties of zirconia ceramics are taken from Eldridge et al. [36] ranging from wavelength 1.2 μm to 7.6 μm. In order to focus the research on the porous struts, the foam porosity, cell diameter and foam sheet thickness are given as a fixed value, where $p_f = 0.85$, $d_c = 3$ mm and $L_f = 10$ mm.

3.1. Alumina foam sheets

Figure 6 shows the apparent radiative properties of alumina foam sheets with different strut porosities p_s. Let's focus on the influence of the second-order pores i.e., the porous struts. It can be found that the spectral absorptance increases with the increase of strut porosity, especially in the wavebands from 0.4 μm to 5.5 μm. At the same time, the spectral transmittance and reflectance decrease with the increase of strut porosity. Within the investigated wavebands from 0.4 μm to 7.0 μm, the total absorptance of foams with strut porosities $p_s = 0.3$, 0.2 and 0.1 (dual-scale-pore foam) are 62.7%, 42.2%, and 20.1% higher than that of $p_s = 0$ (single-scale-pore foam). The data within corresponding wavebands are listed in Table 1. The dual-scale pores (actually the porous struts) cause the incident radiation to undergo more reflection-refraction-scattering-absorption events in the foam volume, thus increasing the possibility of the radiation energy being absorbed. As a result, the radiation absorption is enhanced in the investigated wavebands.

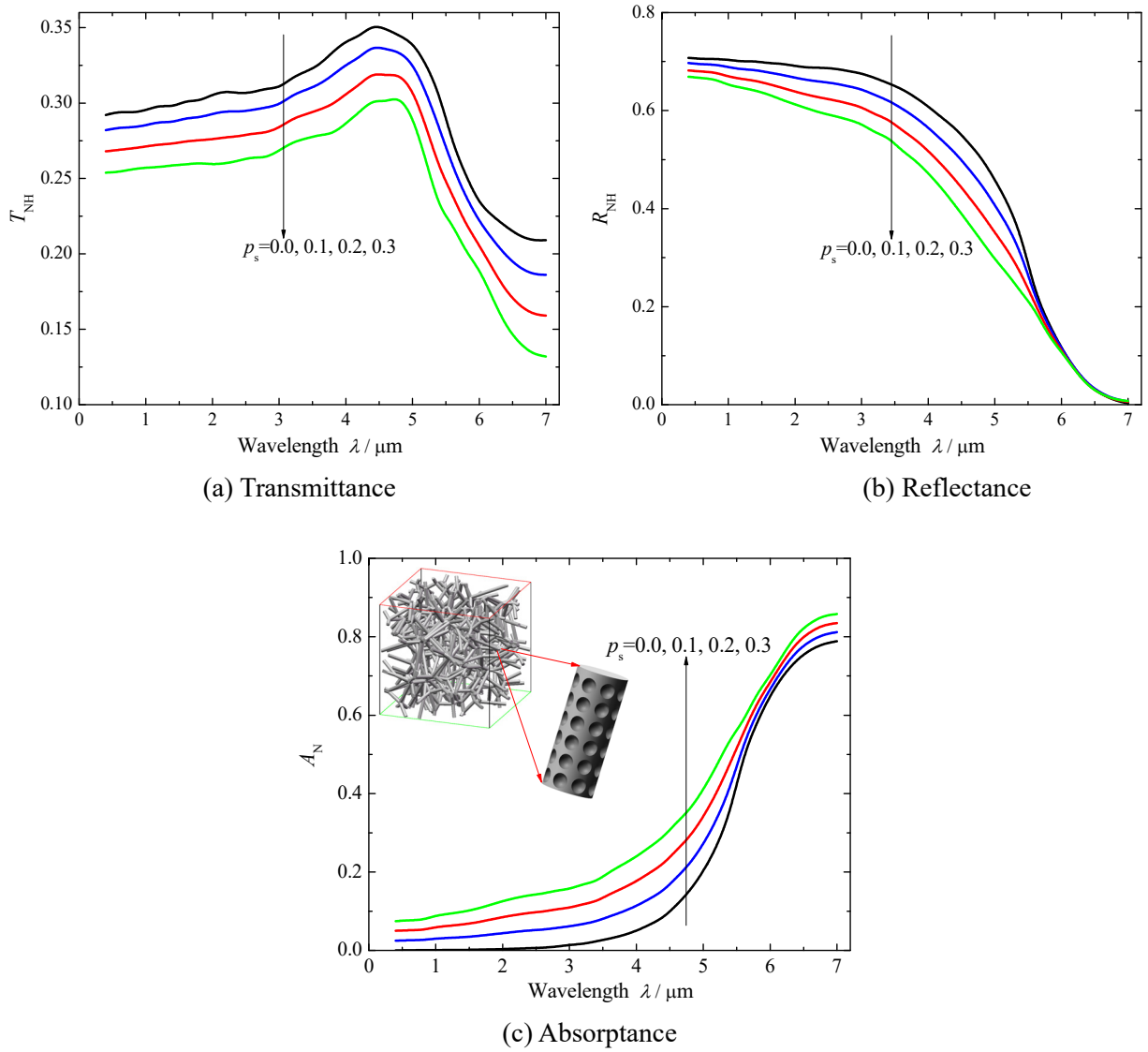

Figure 6. Apparent radiative properties of alumina foam sheets with different strut porosities p_s.

Table 1. Apparent radiative properties of foam sheets within the investigated wavebands.

Foam	Waveband	p_s	T_{NH}	R_{NH}	A_N
Alumina foam	0.4–7.0 μm	0	0.296	0.499	0.204
		0.1	0.280	0.475	0.245
		0.2	0.264	0.447	0.290
		0.3	0.246	0.420	0.332
Zirconia foam	1.2–7.6 μm	0	0.285	0.646	0.069
		0.1	0.274	0.631	0.094
		0.2	0.262	0.616	0.122
		0.3	0.253	0.597	0.149

3.2. Zirconia foam sheets

Figure 7 shows the apparent radiative properties of zirconia foam sheets with different strut

porosities p_s. It can be found that the spectral absorptance increases with the increase of strut porosity, especially in the wavebands from 1.2 μm to 6.5 μm. At the same time, the spectral transmittance and reflectance decrease with the increase of strut porosity. Within the investigated wavebands from 1.2 μm to 7.6 μm, the total absorptance of foams with strut porosities p_s = 0.3, 0.2 and 0.1 (dual-scale-pore foam) are 115.9%, 76.8%, and 36.2% higher than that of p_s = 0 (single-scale-pore foam). The statistics are listed in Table 1. The findings indicate that the dual-scale pores can obviously improve the radiation absorption of zirconia ceramic foams.

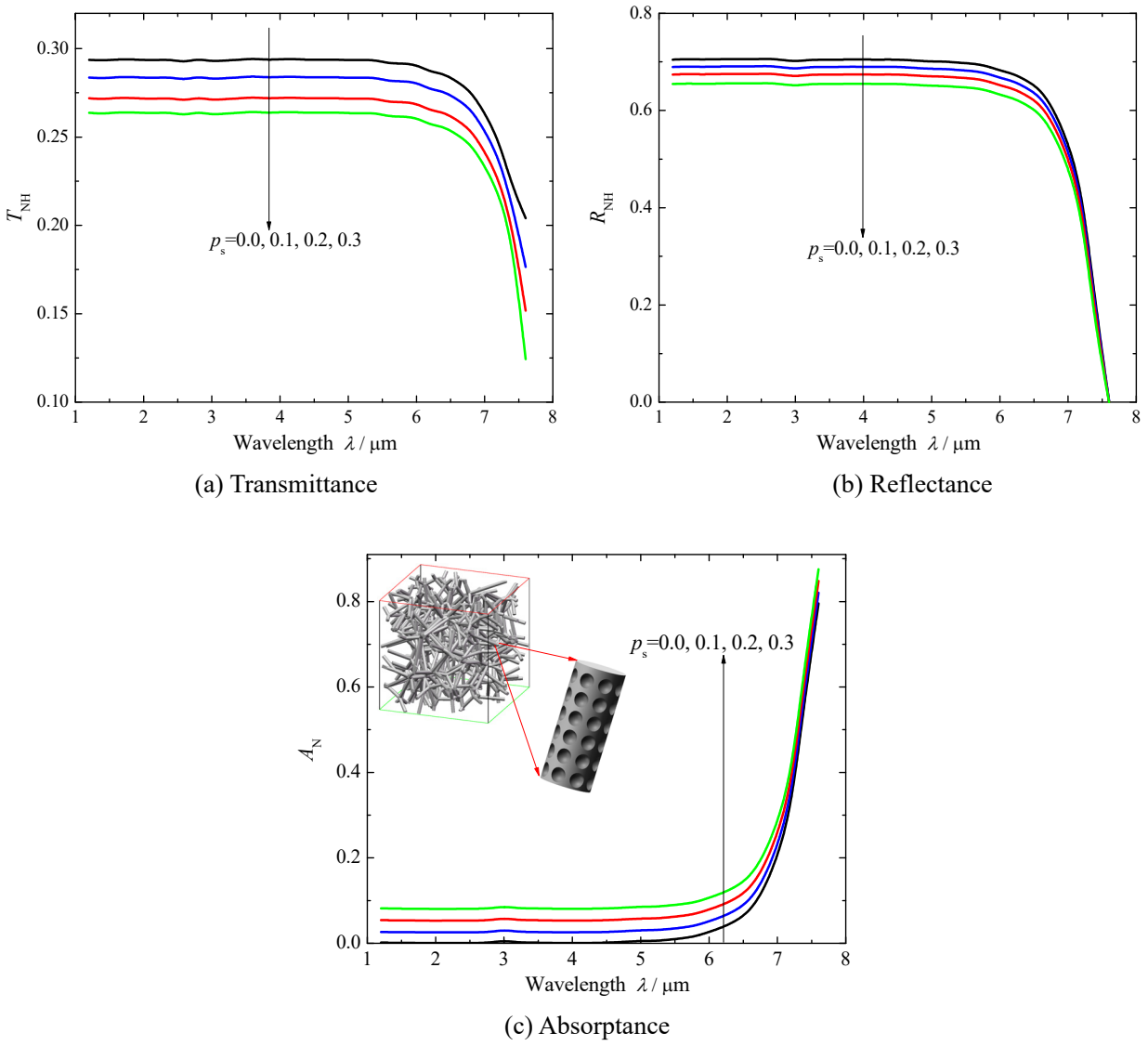

(a) Transmittance

(b) Reflectance

(c) Absorptance

Figure 7. Apparent radiative properties of zirconia foam sheets with different strut porosities p_s.

4. Conclusions

To improve the radiation absorption, open-cell foams with dual-scale pores were digitally designed. The first-order pores are obtained by Voronoi tessellation technique and the second-order pores are described by the 'porous strut'. An in-house Monte Carlo Ray-tracing method is applied in the dual-scale foam structure for radiative transfer calculation. The parameterized study is conducted

on the radiation absorption of alumina foam sheets and zirconia foam sheets, respectively.

The results show that the designed dual-scale alumina foams with strut porosity p_s = 0.3 can increases the normal absorptance within the wavebands from 0.4 μm to 7.0 μm by 62.7% than the foams with single-scale pores. For the zirconia foams, this increase is 115.9% within the wavebands from 1.2 μm to 7.6 μm. The findings can provide strong confidence on dual-scale foams to enhance the absorption of radiation energy in potential applications. Future work will focus on the design of open-cell foams with complex dual-scale pores and on the 3D-printing-based experiments.

Acknowledgments

This work was supported by National Natural Science Foundation of China (Nos. 52006094, 52076064). It was also supported by talent scientific research fund of LSHU (Nos. 2019XJJL-027, 2020XJJL-006).

Conflict of interest

The authors declare no conflict of interest.

References

1. Arif MSB, Uvais M, Shahrin BMA (2020) Extensively used conventional and selected advanced maximum power point tracking techniques for solar photovoltaic applications: An overview. *AIMS Energy* 8: 935–958.
2. Liu XL, Xuan YM (2017) Full-spectrum volumetric solar thermal conversion via photonic nanofluids. *Nanoscale* 9: 14854.
3. Si M, Cheng Q, Zhang Q, et al. (2019) Study of temperature, apparent spectral emissivity, and soot loading of a single burning coal particle using hyper-spectral imaging technique. *Combust Flame* 209: 267–277.
4. Li Y, Chen HW, Xia XL, et al. (2020) Prediction of high-temperature radiative properties of copper, nickel, zirconia, and alumina foams. *Int J Heat Mass Tran* 148: 119154.
5. He YL, Wang K, Qiu Y, et al. (2019) Review of the solar flux distribution in concentrated solar power: non-uniform features, challenges, and solutions. *Appl Therm Eng* 149: 448–474.
6. Wang FQ, Tan JY, Jin HJ, et al. (2015) Thermochemical performance analysis of solar driven CO_2 methane reforming. *Energy* 91: 645–654.
7. Wang FQ, Tan JY, Wang Z (2014) Heat transfer analysis of porous media receiver with different transport and thermophysical models using mixture as feeding gas. *Energy Convers Manage* 83: 159–166.
8. Ma LX, Tan JY, Zhao JM, et al. (2017) Dependent scattering and absorption by densely packed discrete spherical particles: Effects of complex refractive index. *J Quant Spectrosc Ra* 196: 94–102.
9. Barreto G, Canhoto P, Collares-Pereira M (2020) Combined experimental and numerical determination of the asymmetry factor of scattering phase functions in porous volumetric solar receivers. *Sol Energy Mat Sol* C 206: 110327.

10. Li D, Zheng Y, Li Z, et al. (2015) Optical properties of a liquid paraffin-filled double glazing unit. *Energy Build* 108: 381–386.
11. Ma LX, Tan JY, Zhao JM, et al. (2017) Multiple and dependent scattering by densely packed discrete spheres: comparison of radiative transfer and Maxwell theory. *J Quant Spectrosc Ra* 187: 255–266.
12. Arıcı M, Tütüncüa E, Yıldız Ç, et al. (2020) Enhancement of PCM melting rate via internal fin and nanoparticles. *Int J Heat Mass Tran* 156: 119845.
13. Wang BX, Zhao CY (2018) Effect of dependent scattering on light absorption in highly scattering random media. *Int J Heat Mass Tran* 125: 1069–1078.
14. Xia BQ, Pan ZH, Yan J, et al. (2019) Mesoscopic exploration on mass transfer in porous thermochemical heat storage materials. *Int J Heat Mass Tran* 135: 52–61.
15. Li Y, Xia XL, Sun C, et al. (2019) Volumetric radiative properties of irregular open-cell foams made from semitransparent absorbing-scattering media. *J Quant Spectrosc Ra* 224: 325–342.
16. Coquard R, Rousseau B, Echegut P, et al. (2012) Investigations of the radiative properties of Al-NiP foams using tomographic images and stereoscopic micrographs. *Int J Heat Mass Tran* 55: 1606–1619.
17. Barreto G, Canhoto P, Collares-Pereira M (2020) Parametric analysis and optimisation of porous volumetric solar receivers made of open-cell SiC ceramic foam. *Energy* 200: 117476.
18. Herdering A, Abendroth M, Gehre P, et al. (2019) Additive manufactured polyamide foams with periodic grid as templates for the production of functional coated carbon-bonded alumina foam filters. *Ceram Int* 45: 153–159.
19. Li Y, Xia XL, Sun C, et al. (2019) Radiative characteristics of Voronoi open-cell foams made from semitransparent media. *Int J Heat Mass Tran* 133: 1008–1018.
20. Wejrzanowski T, Skibinski J, Szumbarski J, et al. (2013) Structure of foams modeled by Laguerre-Voronoi tessellations. *Comp Mater Sci* 67: 216–221.
21. Pelanconi M, Barbato M, Zavattoni S, et al. (2019) Thermal design, optimization and additive manufacturing of ceramic regular structures to maximize the radiative heat transfer. *Mater Design* 163: 107539.
22. Furler P, Scheffe J, Marxer D, et al. (2014) Thermochemical CO_2 splitting via redox cycling of ceria reticulated foam structures with dual-scale porosities. *Phys Chem Chem Phys* 16: 10503–10511.
23. Barreto G, Canhoto P, Collares-Pereira M (2019) Three-dimensional CFD modelling and thermal performance analysis of porous volumetric receivers coupled to solar concentration systems. *Appl Energy* 252: 113433.
24. Li D, Wu YY, Wang BC, et al. (2020) Optical and thermal performance of glazing units containing PCM in buildings: A review. *Constr Build Mater* 233: 117327.
25. Guévelou S, Rousseau B, Domingues G, et al. (2017) A simple expression for the normal spectral emittance of open-cell foams composed of optically thick and smooth struts. *J Quant Spectrosc Ra* 189: 329–338.
26. Li Y, Xia XL, Sun C, et al. (2018) Tomography-based radiative transfer analysis of an open-cell foam made of semitransparent alumina ceramics. *Sol Energy Mat Sol C* 188: 164–176.
27. Wang FQ, Cheng ZM, Tan JY, et al. (2017) Progress in concentrated solar power technology with parabolic trough collector system: A comprehensive review. *Renewable Sustainable Energy Rev* 79: 1314–1328.

28. Zheng H, Zhu Z, Liu XL (2019) Full-spectrum solar energy allocation for efficient space-based photovoltaic—thermoelectric energy conversion. *J Photon Energy* 9: 032715.
29. Li Y, Chen HW, Wang FQ, et al. (2021) A development to determine spectral radiative properties of semitransparent struts of open-cell ceramic foams: From macro-scale measurement to pore-scale simulation. *Infrared Phys Technol* 113: 103646.
30. Li Y, Xia XL, Sun C, et al. (2018) Tomography-based analysis of apparent directional spectral emissivity of high-porosity nickel foams. *Int J Heat Mass Tran* 118: 402–415.
31. Howell JR, Siegel R, Menguc MP (2011) *Thermal Radiation Heat Transfer*, 5 Eds., Boca Raton: CRC Press.
32. Wang D, Cheng Q, Zhuo X, et al. (2019) Effects of surface emissivity and medium scattering albedo on the computational accuracy of radiative heat transfer by MCM. *J Quant Spectrosc Ra* 240: 106712.
33. Akolkar A, Petrasch J (2011) Tomography based pore-level optimization of radiative transfer in porous media. *Int J Heat Mass Tran* 54: 4775–4783.
34. Li Y, Xia XL, Chen X, et al. (2016) Simulation study on accelerated pore-scale radiative transfer of Ni foam. *Acta Optica Sinica* 36: 1124001.
35. Yang P, Cheng Q, Zhang Z (2017) Radiative properties of ceramic Al_2O_3, AlN and Si_3N_4—II: Modeling. *Int J Thermophys* 38: 124.
36. Eldridge JI, Spuckler CM, Markham JR (2009) Determination of scattering and absorption coefficients for plasma-sprayed yttria-stabilized zirconia thermal barrier coatings at elevated temperatures. *J Am Ceram Soc* 92: 2276–2285.

AIMS Press